Scientific Journal of Silesian University of Technology. Series Transport
Zeszyty Naukowe Politechniki Śląskiej. Seria Transport

Volume 130 **2026**

p-ISSN: 0209-3324

e-ISSN: 2450-1549

DOI: https://doi.org/10.20858/sjsutst.2026.130.15

Journal homepage: http://sjsutst.polsl.pl

Article citation information:
Vilchez, A., Rodriguez, C.V., Cervan, D. Conceptual design of an unmanned aerial vehicle with a fire extinguisher ball dropping system for forest firefighting. *Scientific Journal of Silesian University of Technology. Series Transport*. 2026, **130**, 257-283. ISSN: 0209-3324. DOI: https://doi.org/10.20858/sjsutst.2026.130.15

Antonio VILCHEZ[1], Christian Vladimir RODRIGUEZ[2], Dheybi CERVAN[3]

CONCEPTUAL DESIGN OF AN UNMANNED AERIAL VEHICLE WITH A FIRE EXTINGUISHER BALL DROPPING SYSTEM FOR FOREST FIREFIGHTING

Summary. This study presents the conceptual design of a fixed-wing Unmanned Aerial Vehicle (UAV) equipped with a fire-extinguishing ball deployment system for forest firefighting. The UAV design includes a wingspan of 3.250 m and a length of 3.075 m, using the NACA 6412 airfoil and a high-wing configuration to enhance aerodynamic stability. The fuselage and tail dimensions, including horizontal and vertical stabilizers, were optimized for aerodynamic efficiency. The UAV carries a payload of 13.5 kg, consisting of nine fire-extinguishing balls with a diameter of 152 mm each, providing a total effective coverage area of approximately 90 m². This configuration enables rapid and targeted suppression of ignition points in remote areas affected by wildfires during their growth or declining stages. Aerodynamic performance was evaluated using Computational Fluid Dynamics (CFD) simulations at 30 m/s and angles of attack (AoA) of 0°, 5°, 10°, 15°, and 20°. The UAV achieves a maximum take-off weight of 76.5 kg at an optimal AoA of 7.73°, while the best lift-to-drag ratio (L/D = 29.165) occurs at 5°. Pressure and velocity contours confirm stable flight up to 10° AoA, with stall

---

[1] Universidad Tecnológica del Perú, 15046 Lima, Perú. Email: U17204123@utp.edu.pe. ORCID: https://orcid.org/0009-0009-9917-6455
[2] Universidad Tecnológica del Perú, 15046 Lima, Perú. Email: C25183@utp.edu.pe. ORCID: https://orcid.org/0000-0002-1536-0557
[3] Faculty of Mechanical Engineering, National University of Engineering, Lima, Peru. Email: dcervanp@uni.pe. ORCID: https://orcid.org/0000-0002-2566-3180

behavior starting between 15° and 20°. Operational feasibility was assessed for remote regions such as the Amazon, with a take-off distance of 214.3 m and 317.2 m required to clear a 50-ft obstacle. These results demonstrate that the UAV can safely and efficiently deliver fire-extinguishing payloads in areas with limited accessibility, reducing the need for manned firefighting aircraft and providing a safer alternative for forest fire management.

Keywords: fire extinguisher ball system, firefighting UAV, CFD, conceptual design

1. INTRODUCTION

Wildland fires represent a complex environmental and technological challenge that demands rapid detection, precise intervention, and efficient resource allocation. The suppression of these events involves not only logistical coordination but also the deployment of aerial systems capable of operating under unstable atmospheric conditions, elevated temperatures, and difficult terrain.

In September 2024, Peru recorded 180 forest fires across the regions of Amazonas, Cajamarca, San Martín, Apurímac, Piura, Ucayali, and La Libertad. Traditionally, firefighting efforts rely on the use of water buckets attached to Mi-17 helicopters, which collect water from nearby lakes or rivers. However, the Peruvian Army operates only 16 helicopters, while the Air Force has 9, making it difficult to address this growing challenge effectively [1]. A straightforward solution would be to purchase additional firefighting helicopters, particularly Mi-17 units. Nevertheless, with an estimated cost of 32 million dollars per aircraft, such an investment represents a considerable financial burden, especially when the helicopters would be dedicated solely to this purpose. This limitation raises the following research question: What is the most suitable conceptual design for an unmanned aerial vehicle capable of assisting in forest fire suppression?

In recent years, advances in unmanned aerial technology have opened new possibilities for supporting firefighting strategies through autonomous monitoring, targeted suppression, and reduced exposure of human crews to hazardous environments. Sevzinski et al. [2] determined that only three Mi-17 helicopters equipped with Bambi Buckets are required to extinguish a 240 m² fire. Sousa and Gamboa [3] developed a forest fire detection algorithm implemented on an Unmanned Aerial Vehicle (UAV) equipped with video cameras to identify high-risk areas. Similarly, Wu et al. [4] presented a mathematical model to estimate the optimal number of drones needed to suppress forest fires in suburban areas of Hangzhou, China. Results from 72 simulations indicated an 8% reduction in fire-related losses. Kau et al. [5] proposed the conceptual design of a firefighting helicopter named "FireWasp," featuring a 15.2 m wingspan and 4.2 m height, remotely controlled and capable of carrying up to 730 tons of water. Sharma [6] integrated a fire-extinguishing ball system into a rotary-wing UAV, which received a 97.22% approval rating in its evaluation. Pawar et al. [7] designed a hexacopter equipped with a high-resolution camera and a ball-based fire suppression system capable of collecting and deploying extinguishing spheres. De Moura [8] proposed the use of combat UAVs equipped with thermal cameras to detect potential fire hazards. Dieteren [9] identified several business cases for UAV-based firefighting applications, suggesting the deployment of UAV swarms equipped with cameras, fire-extinguishing ball systems, and detection sensors ("sniffers"). Furthermore, Aydin et al. [10] examined the potential of integrating fire-extinguishing balls into a drone-based system supported by remote sensing technologies as a complement to traditional firefighting. Their proposed system consists of three UAV types: a scouting UAV to detect fires and monitor risks near infrastructure or firefighting brigades, a communication UAV to maintain coordination, and an extinguishing UAV capable of autonomously releasing heat-activated, eco-friendly fire-extinguishing balls.

For this reason, designing a UAV platform for forest fire suppression in different regions of Peru is particularly relevant, as it offers a considerably lower cost compared to acquiring dedicated firefighting aircraft. Moreover, UAVs provide a safer and more accessible alternative, reducing the risks faced by firefighters in hazardous environments. Unlike manned helicopters, UAVs do not require an onboard pilot, since they can be remotely operated. Previous studies suggest that fire-extinguishing spheres are often more effective than water-based methods, as the use of Bambi Buckets depends on the availability of nearby water sources, an impractical condition for most UAVs.

The primary objective of this work is to propose the conceptual design of a fixed-wing UAV equipped with a fire-extinguishing sphere release system for forest firefighting. Specifically, this study develops the aerodynamic design parameters of the UAV, designs the sphere release mechanism, and performs Computational Fluid Dynamics (CFD) simulations at different angles of attack (AoA = 0°, 5°, 10°, 15°, and 20°) and at an air speed of 30 m/s to determine lift (C_y) and drag (C_x) coefficients.

This research offers both practical and academic contributions. From an operational perspective, it provides the Peruvian Air Force with an alternative to reduce reliance on helicopters during firefighting operations. From an academic perspective, it contributes to UAV innovation by integrating aerodynamic analysis, CAD modeling, and CFD simulations. The knowledge generated may guide the development of next-generation firefighting UAVs, particularly for deployment in remote areas that are inaccessible to conventional methods.

2. METHODOLOGY

2.1. UAV aerodynamic design

The conceptual design of the UAV is based on aerodynamic design equations that depend on the aircraft's geometry. For this reason, a set of formulas was selected to calculate the main aerodynamic characteristics of the proposed system, following the methodology described by Artamonova et al. [11]. The geometric parameters were determined for the primary UAV components, namely the wing, fuselage, horizontal stabilizer and vertical stabilizer.

2.1.1. Case study

The proposed UAV is intended for operation in jungle environments affected by wildfires in their growth or declining stages. However, in this study, it is specifically adapted for extinguishing fires in remote and spatially constrained areas characterized by limited water availability and dense vegetation. The selected case study area is Mariscal Cáceres, located in the San Martín region of Peru. This zone lies at an altitude between 350 and 450 m.a.s.l., with high forest density, restricted ground access, and mountainous terrain, which prevents the use of vehicles by firefighters. Due to the scarcity of water sources in the region, the "Bambi Bucket" method would be ineffective for combating the wildfires frequently reported by Aliaga Nestares et al. [12].

2.1.2. Geometric wing parameters

The wing aspect ratio (λ) is defined as the ratio between the squared of the wingspan (l, m) and the wing surface area (s, m^2).

$$\lambda = \frac{l^2}{s} \tag{1}$$

The thickness-to-chord (η) is the relation between the wing root chord (b_{ra}, m) and the wing tip chord (b_{pa}, m).

$$\eta = \frac{b_{ra}}{b_{pa}} \tag{2}$$

The quarter-chord sweep angle ($x_{1/4}$, deg) is a parameter that depends on λ and η. This angle is required for the calculation of the C_y and C_x polar curve.

$$\tan x_{1/4} = \tan x_{ba} - \frac{(\eta - 1)}{\lambda(\eta + 1)} \tag{3}$$

#12#

$$S_w = l \frac{b_{ra} + b_{pa}}{2} \tag{4}$$

Where S_w is the wing area (m^2).

2.1.3. Geometric parameters for horizontal and vertical stabilizers

The horizontal (λ_{eh}) and vertical (λ_{ev}) stabilizer aspect ratios are calculated in the same manner as for ʎ, using the square of the horizontal (l_{eh}, m) and vertical (l_{ev}, m) stabilizer spans, and the horizontal (s_{eh}, m^2) and vertical (s_{ev}, m^2) stabilizer surface areas, respectively.

$$\lambda_{eh} = \frac{l_{eh}^{\ 2}}{s_{eh}} \tag{5}$$

#12#

$$\lambda_{ev} = \frac{l_{ev}^{\ 2}}{s_{ev}} \tag{6}$$

Next, the horizontal (η_{eh}) and vertical (η_{ev}) stabilizer thickness-to-chord ratios and the quarter-chord sweep angle of the horizontal ($H_{1/4}$, deg) and vertical ($V_{1/4}$, deg) stabilizers are computed.

$$\eta_{eh} = \frac{b_{reh}}{b_{peh}} \tag{7}$$

$$\eta_{ev} = \frac{b_{rev}}{b_{pev}} \tag{8}$$

$$\tan H_{1/4} = \tan H_{ba} - \frac{(\eta_{eh} - 1)}{\lambda_{eh}(\eta_{eh} + 1)} \tag{9}$$

$$\tan V_{1/4} = \tan V_{ba} - \frac{(\eta_{ev} - 1)}{\lambda_{ev}(\eta_{ev} + 1)} \tag{10}$$

Where b_{reh} and b_{rev} are the wing root chords of the horizontal and vertical stabilizers (m), and b_{peh} and b_{pev} are the wing tip chords of the horizontal and vertical stabilizers (m).

2.1.4. Geometric parameters for fuselage

The fuselage aspect ratio (λ_f) is defined as the ratio between the fuselage length (l_f, m) and the fuselage diameter (d_f, m).

$$\lambda_f = \frac{l_f}{d_f} \tag{11}$$

The wet fuselage area (S_{mf}, m^2) is defined as the exposed surface of the fuselage once assembled with the other components (wing and tail). It is estimated using d_f, λ_f and l_f.

$$S_{mf} = \pi d_f l_f \left(1 - \frac{2}{\lambda_f}\right)^{2/3} \left(1 + \frac{1}{\lambda_f^2}\right) \tag{12}$$

2.1.5. Aerodynamic parameters

To construct the polar curve, it is necessary to determine the estimated UAV velocity (V_r, m/s), which is obtained from the product of the critical Mach number (M^*) and the speed of sound at the estimated cruise altitude of the UAV (v_h, m/s).

$$V_r = M^* v_h \tag{13}$$

M^* refers to the estimated flight condition at which the airflow over a portion of the wing first reaches the speed of sound. This parameter is determined using the thickness to chord ratio (t_m / c), the relative Mach number ($\overline{M}$) and the mean aerodynamic chord ($\overline{c}$, m). t_m and c are the maximum airfoil thickness (m) and local chord length (m), respectively.

$$\overline{c} = \frac{c}{b} = \frac{0.3}{M^*}\left(\frac{1}{M^* \cos x_{1/4}} - M^* \cos x_{1/4}\right)^{1/3}\left(1 - \left(\frac{5 + \left(M^* \cos x_{1/4}\right)^2}{5 + \overline{M}^2}\right)^{3.5}\right)^{2/3} \tag{14}$$

b is calculated based on the relations previously defined. $\overline{M}$ is calculated using the wing profile coefficient (κ) and the relative wing lift coefficient (C_{ya}).

$$b = \frac{4}{3}\frac{s}{l}\left(1 - \frac{\eta}{(\eta + 1)^2}\right) \tag{15}$$

$$\overline{M} = \kappa - \frac{0.25 C_{ya}}{\cos^2\left(x_{1/4}\right)} \tag{16}$$

Based on these parameters, the polar curve for C_y and C_x can be calculated for UAV cruise flight. The incidence angle (α_0, deg) varies depending on the specific UAV configuration.

$$C_x = C_{x,\min} + a\left(C_y - \left(\frac{\alpha_0}{2a}\right)\right)^2 \tag{17}$$

The blade polar coefficient (a) requires the effective wing aspect ratio ($\lambda_{a\phi}$).

$$a = \frac{1}{\pi \lambda_{a\phi}} \tag{18}$$

2.2. Fire extinguisher ball system design

2.2.1. Maximum take-off weight

It is necessary to calculate the maximum take-off weight ($MTOW$, N) to properly design the ball release system.

$$MTOW = W_0 = W_{payload} + W_{fuel} + W_{empty} \tag{19}$$

Where $W_{payload}$ is the cargo load (N), i.e., the fire-extinguishing balls in this case, W_{fuel} is the fuel mass (N), and W_{empty} represents the empty weight of the UAV (N), as described by Raymer [13]. The calculation of the $MTOW$ depends on the mission profile, defined as the complete distance the UAV must cover from the base to the fire-affected area, where the spheres are released, and then back to the base. Figure 1 illustrates the UAV mission profile, which begins at the base, climbs to cruising altitude, descends to the fire area to release the balls, ascends again to return to the base, recharges the cabin compartment, and then repeats the mission cycle.

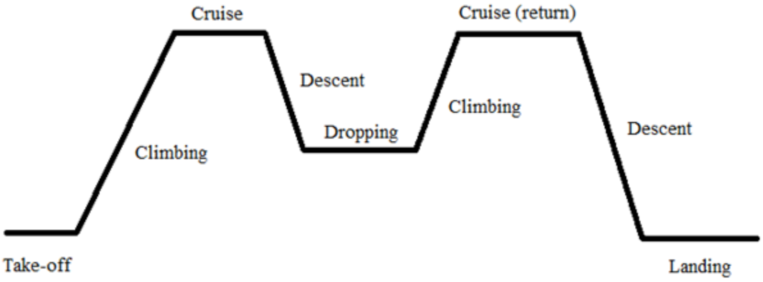

Fig. 1. UAV mission profile

To determine W_{fuel} and W_{empty}, it is necessary to express them as fractions of the take-off weight (W_0, N), as shown in the following equation.

$$W_0 = W_{payload} / \left[1 - \left(W_{fuel} / W_0\right) - \left(W_{empty} / W_0\right)\right] \tag{20}$$

To determine W_{empty} / W_0, historical data are used.

$$W_{empty} / W = KAW_0^B \tag{21}$$

Where K represents the UAV material; its value is 0.95 for composite and 1 for aluminum. In this research, composite material is selected for the design and CFD analysis, as it represents 95% of the weight of an aluminum UAV [14]. A and B coefficients are selected according to the UAV model design. Table 1 presents the values of A and B coefficients used to estimate W_{empty} / W_0.

Tab. 1
A and B coefficients for different aircraft models [14]

Aircraft model	A	B
Glider – powered	0.83	-0.05
Glider - no powered	0.88	-0.05
Homebuilt - metal / wood	1.11	-0.09
Homebuilt - composite	1.07	-0.09
General aviation - single engine	2.05	-0.18
General aviation - twin engine	1.4	-0.10
Agricultural aircraft	0.72	-0.03
Twin turboprop	0.92	-0.05
Amphibious aircraft	1.05	-0.05

According to Jimenez et al. [15], for a medium-sized fixed-wing UAV, the value of A is 0.96 and the value of B is -0.06, based on historical data. In addition, Diogo and Fernandes [16] estimated W_{empty} / W_0 for 98 medium-sized fixed-wing UAVs with combustion engine propulsion systems, finding values ranging from 0.44 to 0.63. Based on the mission profile,

W_{empty}/W_0 is divided into flight segments. Table 2 presents the corresponding values and equations for each segment.

Tab. 2

Values of W_{empty}/W_0 at different flight segments [16]

Segment	W_{empty}/W_0
1. Take-off	0.970
2. Climbing	0.985
3. Cruise	$\exp\{-RCG/[V_r(L/D)]\}$
4. Descent	1.000
5. Dropping	$\exp\{-RCG/[V_r(L/D)]\}$
6. Climbing	0.985
7. Cruise (base)	$\exp\{-RCG/[V_r(L/D)]\}$
8. Descent	1.000
9. Landing	0.995

Where R is the range (m), C is the specific fuel consumption (kg/N.s), G is the gravitational acceleration (9.81 m/s^2), and L/D is the lift-to-drag ratio, calculated using the wing wet area (S_{wet}, m^2) and S_w.

$$L/D_{\max} = 0.9\sqrt{\lambda/(S_{wet}/S_w)} \tag{22}$$

$$C = C_{power}\frac{V_r}{\eta_P} \tag{23}$$

Where C_{power} is the fuel consumption per unit of power (kg/W.s), and η_P is the propeller propulsive efficiency. The value of η_P is 0.8, while C_{power} is 0.068 kg/kW.h (or 0.2448x10^{-6} kg/W.s) for an internal combustion engine with a constant-speed propeller.

The fuel fraction can be calculated using the following equation.

$$W_{fuel}/W_0 = 1.06(1 - W_N/W_1) \tag{24}$$

Where W_N/W_1 is the fuel fraction, defined as the ratio of the last flight segment to the first segment, depending on the UAV mission profile. A safety factor of 1.06 is applied to ensure an operational fuel reserve.

2.2.2. Fuel tank volume

According to Torenbeek [17], fuel can be stored in the wings, as they are considered large hollow structures suitable for this purpose. Storing fuel inside the wing reduces the bending moment and improves the aircraft's longitudinal balance. Torenbeek estimates the fuel tank volume ($V_{\tan k}$, m^3) using the empirical equation (25).

$$V_{\tan k} = 0.54 S_w^{1.5} \frac{\bar{c}}{b} \frac{1}{\sqrt{\lambda}} \frac{1+\eta\left(\frac{\bar{c}}{b}\right)+\eta^2\left(\frac{\bar{c}}{b}\right)}{(1+\eta)^2} \tag{25}$$

The constant value 0.54 is a structural correction factor derived from statistical aircraft design data.

2.2.3. Engine position and cabin design

A piston engine is planned to be installed in the tail section of the UAV, following a pusher configuration. This configuration, as employed by Chen et al. [18], was found to improve UAV aerodynamic stability and reduce drag during cruise flight. In this study, the proposed engine configuration will not be analyzed through CFD; it is considered solely for the weight calculations discussed before.

For the cabin design, the cabin wall thickness (T_c, m) is determined as the sum of the external fuselage covering thickness (T_f, m), the acoustic insulation thickness (T_a, m) and the structural composite material thickness (T_{cm}, m).

$$T_c = T_f + T_a + T_{cm} \tag{26}$$

The initial interior diameter (I_d, m) depends on T_c and the initial ramp height (I_r, m). I_r represents the vertical ramp height required to guide the fire-extinguishing spheres toward the release door.

$$I_d = d_f - 2T_c - I_r \tag{27}$$

The interior diameter of the release door (I_{dr}, m) is a geometric parameter that depends on the cabin interior diameter and determines the maximum allowable size of the fire-extinguishing spheres to be released.

$$I_{dr} = d_f - 2T_c \tag{28}$$

2.2.4. Fire extinguisher balls

Fire extinguisher balls are compact devices designed to suppress fires through automatic activation when exposed to open flames. Their outer shell, typically made of PVC to withstand impacts, encloses monoammonium phosphate, which is released by a fusible element upon contact with fire. These spheres are particularly suitable for areas with difficult access and provide an effective extinguishing radius of approximately 3-10 meters, making them especially effective for suppressing wildfires during their growth or decay phases. Among the most widely recognized industrial products are the AFO and Elide fire extinguisher balls, which have already been implemented in rotor UAV applications [19]. Table 3 presents different suppliers of fire extinguisher balls along with their general specifications.

Tab. 3

Specifications of fire extinguisher balls [19]

Supplier	Diameter (mm)	Weight (kg)	Effective area (m^2)	Activation time (s)
Elide Fire	152	1.5	8-10	3–10
TPMCSTEEL FE8802	150	1.3	2.5	3–10
Junani Fire	150	1.3	3.0	5–10
Ketaifire AFO	150	1.5	3.0	3–10
TPMCSTEEL FE8804	226	4.0	9.0	3–10
Ketaifire TY4	215	4.2	9	≤3

2.3. CFD Simulation setup

The continuity and momentum equations are expressed as [20]:

$$\frac{\delta\rho}{\delta t}+\frac{\delta(\rho u)}{\delta x}+\frac{\delta(\rho v)}{\delta y}+\frac{\delta(\rho w)}{\delta z}=0 \tag{29}$$

$$\frac{\delta(\rho u)}{\delta t}+\frac{\delta(\rho u^2)}{\delta x}+\frac{\delta(\rho uv)}{\delta y}+\frac{\delta(\rho uw)}{\delta z}=-\frac{\delta p}{\delta x}+\frac{1}{\mathrm{Re}_r}\left[\frac{\delta\tau_{xx}}{\delta x}+\frac{\delta\tau_{xy}}{\delta y}+\frac{\delta\tau_{xz}}{\delta z}\right] \tag{30}$$

$$\frac{\delta(\rho v)}{\delta t}+\frac{\delta(\rho uv)}{\delta x}+\frac{\delta(\rho v^2)}{\delta y}+\frac{\delta(\rho vw)}{\delta z}=-\frac{\delta p}{\delta y}+\frac{1}{\mathrm{Re}_r}\left[\frac{\delta\tau_{xy}}{\delta x}+\frac{\delta\tau_{yy}}{\delta y}+\frac{\delta\tau_{yz}}{\delta z}\right] \tag{31}$$

$$\frac{\delta(\rho w)}{\delta t}+\frac{\delta(\rho uw)}{\delta x}+\frac{\delta(\rho vw)}{\delta y}+\frac{\delta(\rho w^2)}{\delta z}=-\frac{\delta p}{\delta z}+\frac{1}{\mathrm{Re}_r}\left[\frac{\delta\tau_{xz}}{\delta x}+\frac{\delta\tau_{yz}}{\delta y}+\frac{\delta\tau_{zz}}{\delta z}\right] \tag{32}$$

Where u, v and w represent the velocity components in the x, y and z directions (m/s), respectively. ρ is the fluid density (kg/m^3), p represents the static pressure (Pa), Re_r is the Reynolds number, τ represents the stress tensor (Pa) and t is the time (s).

The Reynolds-Averaged Navier–Stokes (RANS) turbulence model solves the Navier–Stokes equations by modeling part of the turbulent flow, thereby providing an averaged representation of the fluid behavior [20]. For turbulence modeling, the Shear Stress Transport (SST) k-ω model is employed, as it provides improved accuracy in predicting flow separation under adverse pressure gradients. The transport equations for the turbulent kinetic energy (k, m^2/s^2) and the specific dissipation rate (ω, s^{-1}) are expressed as follows:

$$\frac{\delta(\rho k)}{\delta t}+\frac{\delta(\rho k u_i)}{\delta x_i}=\frac{\delta}{\delta x_j}\left(\Gamma_k\frac{\delta k}{\delta x_j}\right)+\tilde{G}_k-Y_k+S_k \tag{33}$$

$$\frac{\delta(\rho\omega)}{\delta t}+\frac{\delta(\rho\omega u_i)}{\delta x_i}=\frac{\delta}{\delta x_j}\left(\Gamma_\omega\frac{\delta\omega}{\delta x_j}\right)+G_\omega-Y_\omega+D_\omega+S_\omega \tag{34}$$

$\widetilde{G}_k$ represents the kinetic energy associated with mean velocity gradients (kg/m.s^3), while G_ω denotes the generation of ω (kg/m^3.s^2). The terms Γ_k and Γ_ω account for the effective diffusivity of k and ω (kg/m.s), respectively. D_ω is the cross-diffusion term (kg/m^3.s^2), whereas Y_k (kg/m.s^3) and Y_ω (kg/m^3.s^2) correspond to the dissipation of k and ω due to turbulence. S_k (kg/m.s^3) and S_ω (kg/m^3.s^2) are user-defined source terms. ANSYS Fluent implements equations (33) and (34) within its SST k-ω model.

A mesh independence study is also required to determine the optimal mesh density for the simulations. The analysis is performed using three meshes: Coarse, Medium, and Fine. The mesh selected for subsequent simulations is the one that yields an error less than or equal to 5%. In this study, the variable of interest for the validation is C_x.

After obtaining the CFD results for lift and drag at different AoA, the wing loading (P, N/m^2) can be estimated using the following expression:

$$P=\frac{MTOW}{S_w} \tag{35}$$

$MTOW$ allows the calculation of the landing weight (W_{land}, N).

$$W_{land}=0.85MTOW \tag{36}$$

This analysis implies that P during the take-off procedure can be estimated based on P in the landing phase (P_{land}, N/m^2).

$$P=\frac{1}{0.85}P_{land} \tag{37}$$

Raymer [13] estimates the runway length (S_{to}, m) from historical data, using the take-off parameter (TOP, N/m^2), which is defined as:

$$TOP=\frac{P}{0.865\left(\frac{T}{MTOW}\right)C_{y,\max}} \tag{38}$$

Where T is the thrust force (N). Once the TOP value is obtained, S_{to} can be expressed as:

$$S_{to}=25TOP \tag{39}$$

The distance required to clear a 50 ft obstacle (S_{50}, m) can be calculated as:

$$S_{50} = 37TOP \tag{40}$$

Based on the calculated values, the required landing distance of the runway (S_{land}, m) is expressed as:

$$S_{land} = 80\frac{P}{C_{y,\max}\sigma} + S_{50} \tag{41}$$

Where σ denotes the relative air density, while the constant 80 is a conversion factor applied when working in imperial units.

3. RESULTS AND DISCUSSION

3.1. UAV aerodynamic design

3.1.1. Reference UAV model

The UAV design was referenced to the Spanish drone "Sirtap" [21], used solely as a baseline. To establish real dimensional references (wing, tail, fuselage), the COMAC C919 aircraft was selected, from which three-view drawings were extracted and scaled to match the Sirtap dimensions, resulting in a unique UAV configuration. This scaling process was performed in Autodesk Inventor using publicly available images of the C919 [22]. Based on this unified scale (see Table 4, last column), several geometric modifications were introduced, including changes to the airfoil profile, wing configuration, and tail design, in order to develop the final UAV model. Moreover, the design integrates a distinctive feature: a front-opening cockpit mechanism inspired by the Antonov AN-225.

Tab. 4
Aerodynamic characteristics of Sirtap, COMAC C919 and designed UAV [21-22]

Characteristics	Sirtap dimensions	C919 dimensions	Designed UAV
Longitude	7.3 m	38.9 m	3.075 m
Wingspan	12 m	35.8 m	3.250 m
Height	2.2 m	11.95 m	0.665 m
MTOW	750 kg	72 500 kg	Not calculated
Payload	180 kg	20 000 kg	13.5 kg
Velocity	200 km/h (M 0.16)	828 km/h (M 0.78)	108 km/h (M 0.08)
Range	2000 km (14 h)	5,555 km	Not calculated
Maximum altitude	6.40 km	12.1 km	5 km (estimated)

A fixed-wing UAV is more suitable for transporting payloads over medium to long distances because of its superior aerodynamic efficiency, extended endurance, and reduced energy demand for lift generation. These characteristics enable a greater proportion of the total weight to be allocated to useful payload [23] (see Table 5 for details).

Tab. 5

Comparison of fixed-wing and rotor-wing UAVs [23]

Characteristics	Fixed wing	Rotor wing
High velocities	Yes	No
Cargo load	Better	Less
Range (h)	Better	Less
Lift effectiveness	Better	Less

3.1.2. Study area

The hypothetical forest fire case study is located in the district of Huicungo, Mariscal Cáceres Province, San Martín, Peru. The estimated affected area is 1 ha, and the distance from the UAV base to the event site is approximately 1.90 km (see Figure 2 for details).

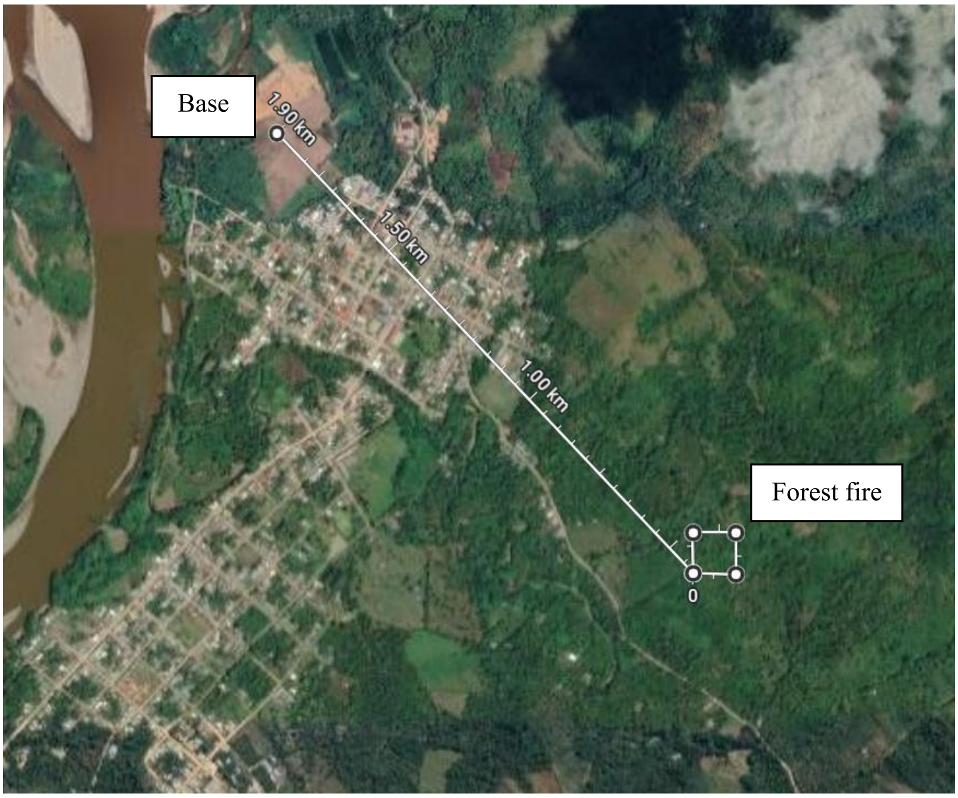

Fig. 2. Hypothetical forest fire scenario in Huicungo, San Martin

3.1.3. Geometric wing parameters

The NACA 6412 airfoil was selected to design the wing due to its ability to generate high lift while maintaining low aerodynamic drag [24]. A swept-back wing configuration was chosen, as it provides improved aerodynamic performance, reduced weight, and simpler construction compared to other wing profiles. The NACA 6412 airfoil performs efficiently at low speeds, offering a high L/D. In comparison, the NACA 2412 (used in the Cessna 172) exhibits a lower L/D ratio at low velocities, as does the Clark Y profile. Additionally, a high-wing configuration was adopted to enhance flight stability, while the high aspect ratio contributes to increased lift. The resulting dimensions are summarized in Table 6.

Tab. 6

Geometric parameters of the wing

Parameter	Dimension	Parameter	Dimension
Wingspan	3.25 m	Thickness to chord ratio	3.17
Wingspan without fuselage	2.65 m	Forward sweep angle	20°
Tip chord	0.17 m	Aft sweep angle	5°
Root chord	0.54 m	¼ Sweep angle	16.69°
Wing to fuselage chord	0.60 m	Average aerodynamic chord	0.38 m
Wing area	1.15 m^2	Average thickness	0.05
Area without fuselage	1.02 m^2	Relative thickness	0.13
Aspect ratio	9.18	Average chord distance	0.67 m

3.1.4. Geometric parameters for stabilizers and fuselage

A "T" configuration for the empennage was selected to minimize aerodynamic interference between the horizontal stabilizer and the fuselage (see details in Table 7). This configuration offers higher pitch efficiency compared to "H" or conventional layouts, as the entire horizontal stabilizer is effective and provides greater surface area for pitch control. Although a "V" configuration can reduce both weight and wetted surface area, it requires a more complex control system and may result in less precise maneuvering due to mixed control inputs [25]. A "T" configuration for the empennage also improves the aerodynamic effectiveness of the vertical stabilizer, enhancing yaw control and providing greater directional stability (see Table 8). Fuselage dimensions are presented in Table 9.

Tab. 7

Geometric parameters of the horizontal stabilizer

Parameter	Dimension	Parameter	Dimension
H.E. span	1.01 m	Thickness to chord	2.39
H.E. span without fuselage	1.01 m	Forward sweep angle	30°
Tip chord	0.18 m	Aft sweep angle	10°
Root chord	0.43 m	¼ Sweep angle	22.78°
H.E. to fuselage chord	0.40 m	Average aerodynamic chord	0.26 m
Area	0.30 m^2	Average thickness	0.03
Area without fuselage	0.32 m^2	Relative thickness	0.09
Aspect ratio	2.68	Average chord distance	0.32

Tab. 8

Geometric parameters of the vertical stabilizer

Parameter	Dimension	Parameter	Dimension
Longitude	0.65 m	Thickness to chord	3.64
Tip chord	0.17 m	Forward sweep angle	40°
Root chord	0.62 m	Aft sweep angle	30°
Area	0.25 m^2	¼ sweep angle	26.56°
Aspect ratio	1.69	Average thickness	0.06
Average aerodynamic chord	0.26 m	Relative thickness	0.13

Tab. 9

Fuselage geometric parameters

Parameter	Dimension	Parameter	Dimension
Longitude	2.775 m	Mid aft diameter	0.18 m
Tip longitude	0.3 m	Mid-section area	0.09 m^2
Aft longitude	0.975 m	Aft section area	0.02 m^2
Diameter	0.34 m	Aspect ratio	8.16

Mid diameter	0.34 m	Tip aspect ratio	0.88
Wet area	2.49 m^2	Aft aspect ratio	1.10

3.1.5. Aerodynamic parameters

$\overline{M}$ was calculated as 1.03 using κ = 1 and C_{ya} = 0.6 (subcritical airfoils). From this, M^* was determined as 0.78, resulting in an V_r of 249.95 m/s. This value represents the maximum attainable speed according to the aerodynamic characteristics and power plant performance. However, for the present research, a reference velocity of V_r = 30 m/s was selected, which will be used for the calculation of the polar curve and for CFD simulations.

3.1.6. UAV CAD design

The fire extinguisher UAV was modeled in Autodesk Inventor, where the principal drawing dimensions were established (see Figure 3).

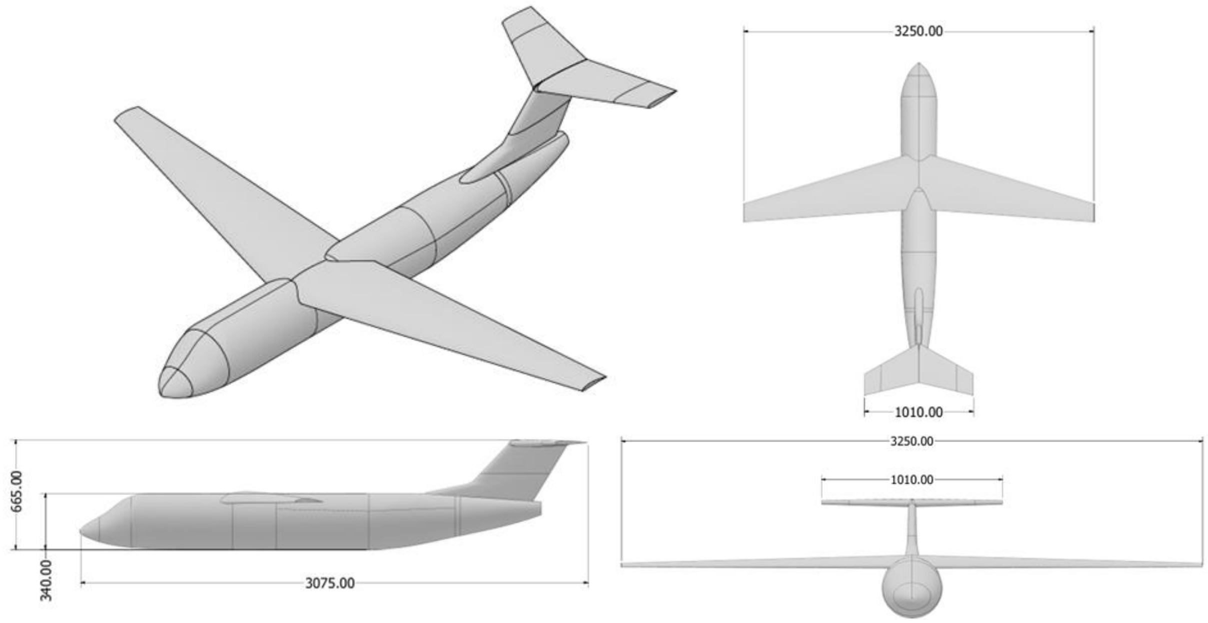

Fig. 3. UAV design in different views (dimensions in mm)

3.1.7. Aerodynamic polar curves

The polar curve, showing the relationship between C_y and C_x, was constructed as seen in Figure 4 (M = 0.08). It can be observed in Figure 4 that as lift increases, aerodynamic drag also rises. However, the drag remains relatively low due to the wing's design characteristics, which contribute to improved stability. Subsequently, Figure 5 presents the relationship between C_y and AoA, where κ is 0.93 and $x_{1/4}$ = 20°.

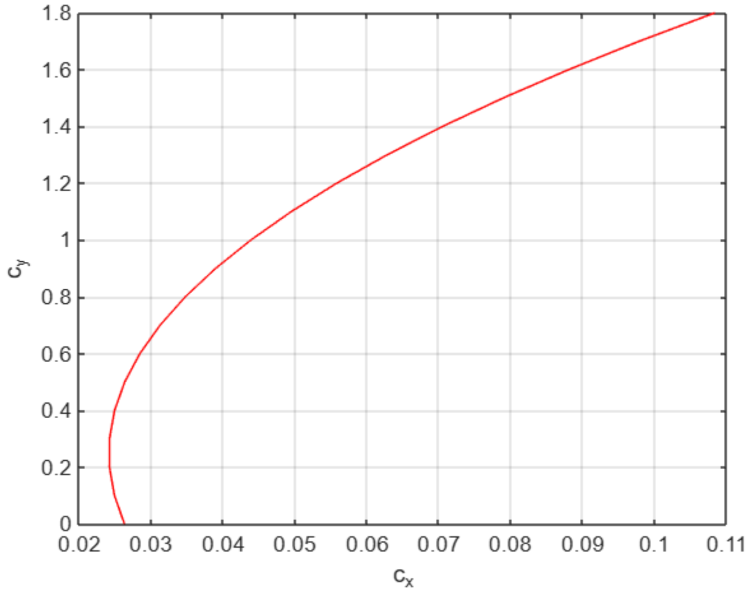

Fig. 4. Lift-drag polar curve

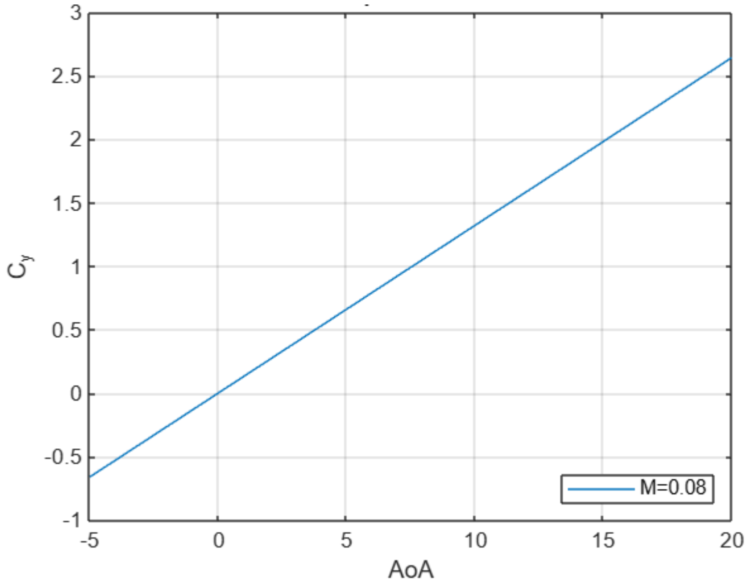

Fig. 5. C_y vs AoA at $M = 0.08$

3.2. Fire extinguisher ball system design

The release system is integrated within the UAV to prevent any alteration of its aerodynamic characteristics or external shape during flight. The fire-extinguishing balls are discharged sequentially, sliding down an internal inclined ramp that ensures their orderly release.

3.2.1. Maximum take-off weight

As shown in Figure 6, the selected UAV mission profile follows the operational role of a bomber aircraft, consisting of nine segments as described in Table 1.

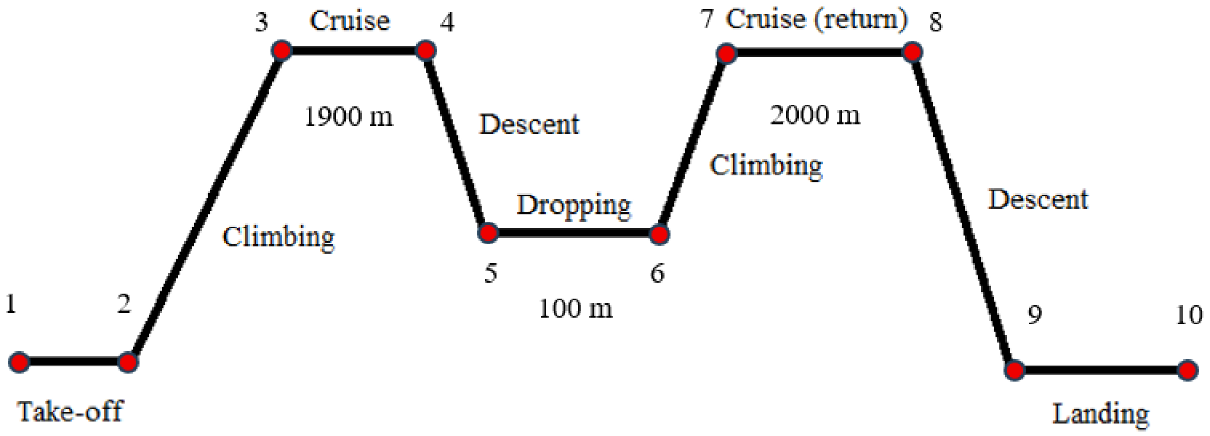

Fig. 6. Actual UAV mission profile

Considering $R = 1900$ m (the hypothetical case on Figure 2), η_P is 0.8 for a constant velocity propeller, and C_{power} is 0.068 mg/Ws. Under these conditions, $MTOW$ is 604.06 N and W_{empty} is 429.97 kg. Based on this weight distribution, W_{fuel} is 4.2255 kg.

The fuel quantity in liters is obtained using the density relationship. According to Zhao and Cui [26], Jet-A fuel is optimal for medium UAVs equipped with piston engines, with a typical density of 804 kg/m^3. Therefore, the required fuel volume for this mission is 5.25 L. For longer ranges, if $R = 10$ km, the fuel requirement increases to 5.3738 kg, and for $R = 90$ km, the maximum operative UAV weight reaches 744.44 N.

3.2.2. Volume of the fuel tank

$V_{\tan k}$, within the wings, is calculated as 23.8 L, corresponding to a maximum fuel weight of 19.14 kg. This fuel capacity allows estimating $MTOW_{op\max} = 750.27$ N. When compared with the $MTOW_{\max}$ obtained in Section 3.2.1, the difference is 0.6305 kg, which represents an additional safety margin of 0.8% on top of the initial 6% considered in equation (25).

3.2.3. Engine position and cabin design

The design parameters calculated for T_c, I_d and I_{dr} are 15, 244 and 314 mm, respectively. $I_l = 1500$ mm is considered, as shown in Figure 7. Additionally, the slot designated for the release door is located beneath the cabin, with dimensions of 400 mm × 200 mm.

3.2.4. Integrated system

Based on the suppliers listed in Table 3, the Elide Fire extinguisher ball (152 mm diameter, 8-10 m^2 effectiveness) was selected for this study (see Figure 8 for the integrated system view). The proposed system consists of nine balls, providing a total suppression coverage of approximately 90 m^2 and a payload weight of 13.5 kg. Accordingly, the UAV will be capable of carrying nine balls, each weighing 1.5 kg, achieving a fire suppression effectiveness of about 9 m^2 per ball over a linear range of 90 meters.

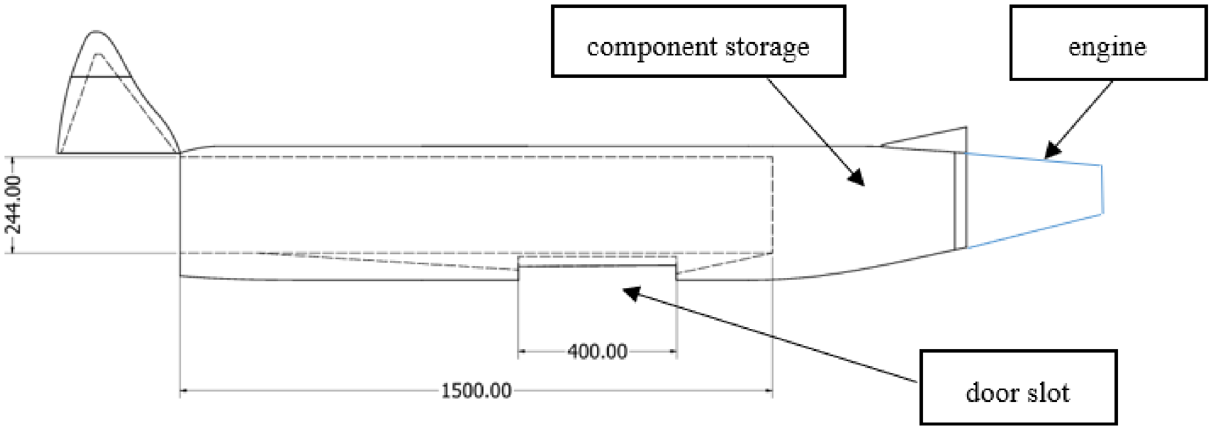

Fig. 7. Cabin geometry (dimensions in mm)

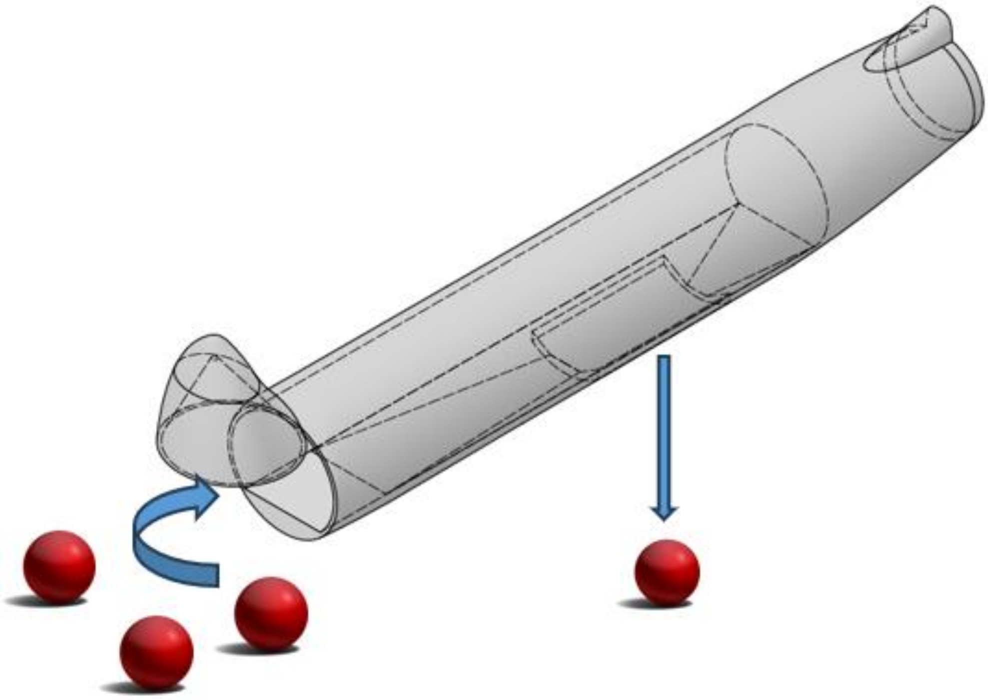

Fig. 8. Integrated fire extinguisher ball system for UAV

Compared with traditional aerial firefighting methods, such as water-dropping aircraft, fire-extinguishing balls do not evaporate upon release and instead activate upon contact with flames, providing localized chemical suppression at high-temperature ignition points. Large aerial tankers can deliver substantially higher volumetric payloads; however, their operability in remote areas is often limited due to the absence of nearby water sources, which increases turnaround time per sortie. Consequently, the operational cycle of large aircraft becomes extended, particularly in regions such as the Peruvian rainforest, where long runways are scarce.

In contrast, the proposed UAV is intended to complement traditional methods by relying on pre-positioned warehouses of fire-extinguishing balls located near high-risk wildfire areas. Table 10 presents a comparison between the proposed UAV and large aerial tankers under the hypothetical forest fire scenario illustrated in Figure 2 for the Huicungo district, San Martín.

Tab. 10

Comparative effectiveness of the proposed UAV and
a large aerial tanker under the Huicungo wildfire scenario

Parameter	UAV (9 balls)	Large aerial tanker
Deployment time (remote areas)	Low	High
Payload mass	13.5 kg	Several thousand kg
Suppression precision	High	Moderate
Operational frequency	High	Low
Optimal deployment phase	Early-stage / spot fires	Fully developed fires

3.3. CFD simulation results

3.3.1. Domain

According to Wibowo et al. [27], the computational domain should be constructed using the aircraft length (3.075 m) as the reference parameter. Figure 9 illustrates the recommended domain dimensions.

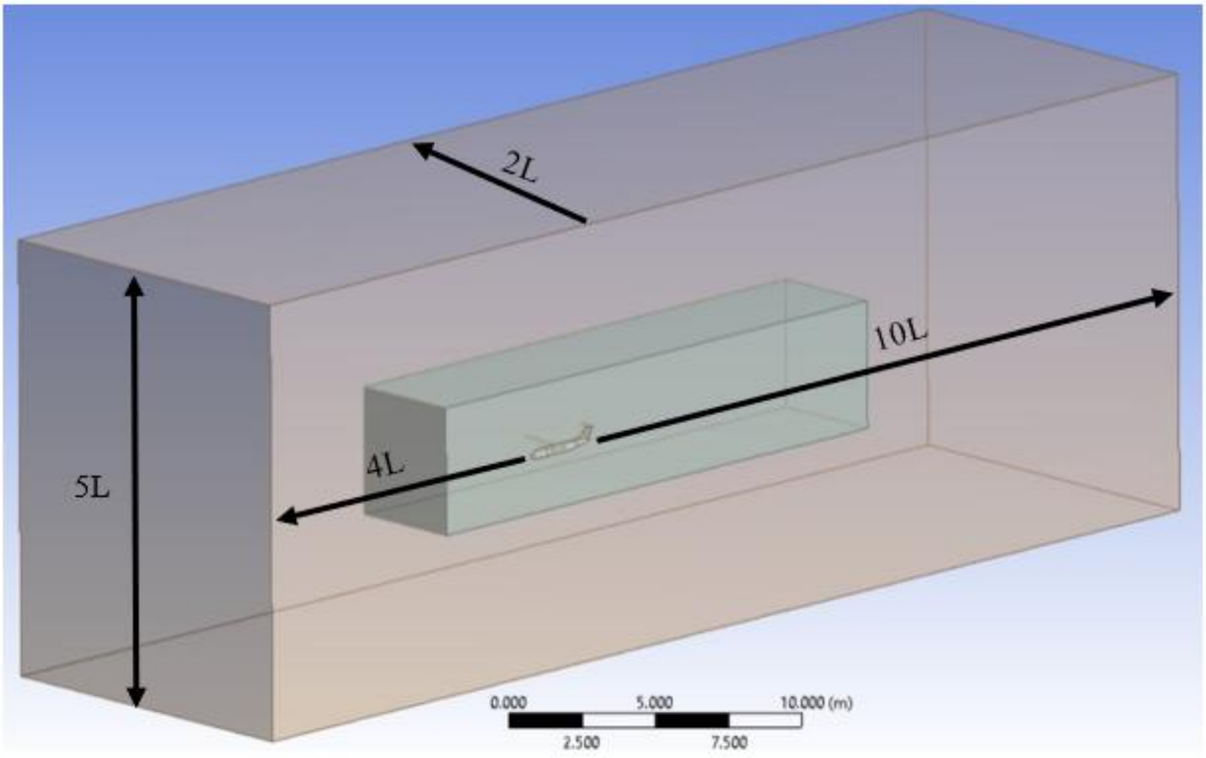

Fig. 9. Computational domain

3.3.2. Meshing

A mesh independence study was conducted to determine the optimal mesh density for the simulations. Table 11 presents the results obtained at AoA = 0°, focusing on the estimation of C_x. The results of the mesh independence study indicated that the medium mesh configuration (6’300 000 cells) was the most suitable for this case, with an average element quality of 0.87 and an error percentage of 5.06% (see Table 11). Local refinements were applied, particularly around the UAV wings and stabilizers (see Figure 10). Therefore, the next aerodynamic simulations at AoA of 0°, 5°, 10°, 15° and 20° were performed using the Medium mesh. Note that Cai et al. [28] recommend using more than 8 million elements for reliable CFD analysis.

Tab. 11

Results of the mesh independence study

Mesh	Cells	C_x	Error
Coarse	3’200 000	0.0134	10.67%
Medium	6’300 000	0.0150	5.06%
Fine	13’200 000	0.0158	

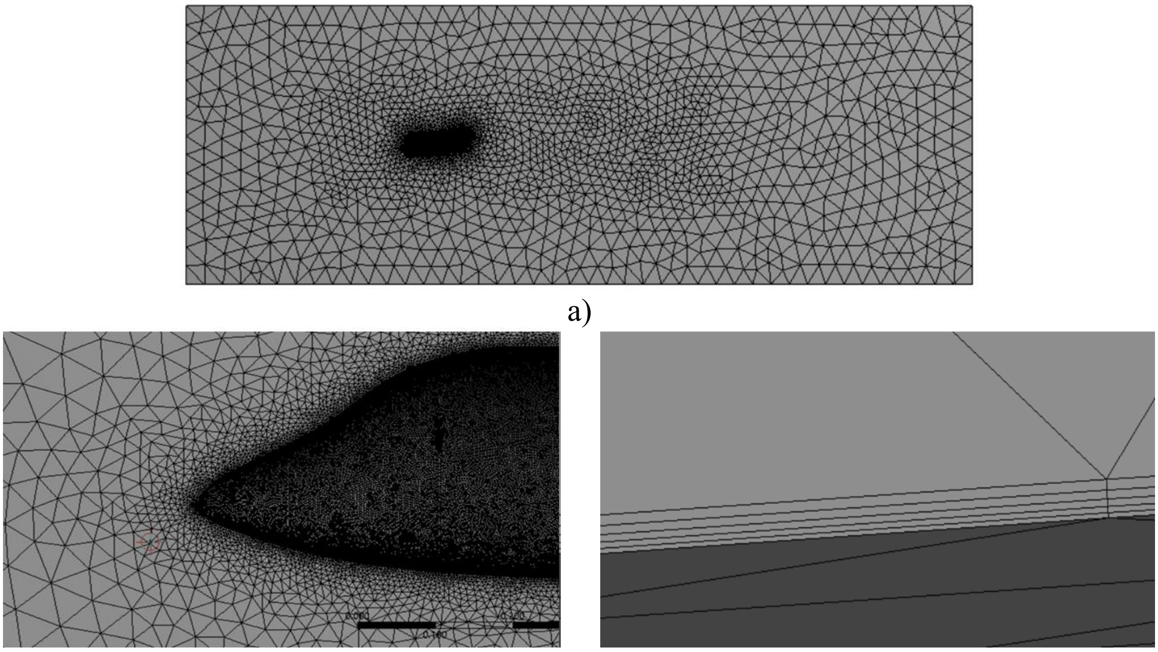

a)

b) c)

Fig. 10. Medium mesh views: a) general domain, b) front of the UAV, and c) boundary layers

3.3.3. Boundary conditions

The velocity inlet was set at 30 m/s (see Figure 11). An altitude of 100 m was considered; however, given that the Peruvian Amazon ranges between 80 m and 400 m, an altitude reference of 500 m was adopted. At this altitude, according to the Standard Atmosphere [29], air density decreases from 1.225 kg/m³ at sea level to 1.167 kg/m³. The air density value at 500 m was selected for the CFD simulations.

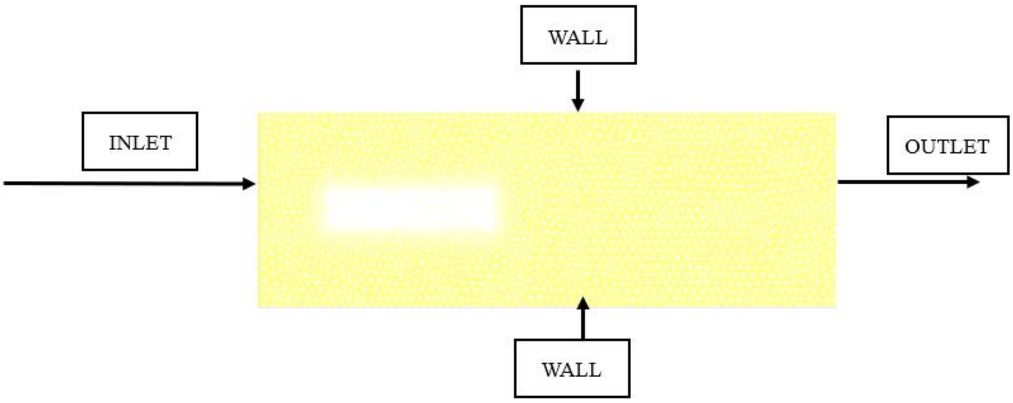

Fig. 11. Boundary conditions

3.3.4. Lift and drag forces

Table 12 presents the calculated aerodynamic forces for AoA of 0°, 5°, 10°, 15° and 20°. As shown in Table 12, the lift force (L) increases with AoA, while drag (D) also increases but to a lesser extent. Considering $MTOW$ for R = 1.9 km, the UAV must generate more than 604.06 N of lift to take off and maintain cruise flight. This condition is reached at approximately 5°-10° AoA, defining the required operational AoA under normal conditions. Although L/D reaches 29.17 at 5°, the generated lift is only 599.09 N, which is insufficient. Therefore, as suggested by Anderson [30], interpolation between 5°-10° is required since the curve in this range is approximately linear. Accordingly, for R = 10 km (W_0 = 615.32 N), the optimal AoA is 5.29°, while for R = 90 km the corresponding AoA is 7.73°.

Tab. 12
Aerodynamic forces at different AoAs

AoA	L (N)	D (N)	L/D
0°	291.800	16.634	17.542
5°	599.078	20.541	29.165
10°	875.720	93.382	9.378
15°	1033.378	177.294	5.828
20°	1012.838	207.498	4.881

P for the maximum operative UAV weight was calculated as 66.53 kgf/m², which according to Raymer [13] indicates a relatively short take-off distance, a favorable result for UAV operations in remote and hard-to-access areas. For landing conditions, W_{land} was determined as 65.03 kgf, giving P = 554.54 N/m². S_{to} was calculated using $C_{y,\max}$ = 1.4 for the NACA 6412 airfoil [24] and $L/MTOW$ = 0.4 from Raymer [13], yielding TOP = 28.13. Based on this, the take-off distance is 214.34 m, while the distance to clear a 50 ft obstacle is 317.23 m. For landing, S_{land} was estimated using the obstacle clearance requirement for UAVs of 50 ft, giving S_{50} = 1040.77 ft, adjusted to the relative air density at 400 m (Huicungo, San Martín). Finally, the thrust required for level flight was determined using $L/MTOW$. For the maximum operative UAV weight, the required thrust is 300.11 N.

3.3.5. Pressure and velocity contours

Pressure contours demonstrated a proportional increase with AoA (see Figure 12). The results show that pressure reaches its maximum values on the intrados, with the magnitude of pressure rising as AoA increases. At 15°, a significant intensification of pressure distribution is observed, while Table 12 indicates L/D decreases between 15° and 20°. Furthermore, at 20° the lift shows a marked reduction, which can be interpreted as the onset of stall. According to Belligoli et al. [31], an effective approach to reduce drag in UAV design is the addition of fairings at the wing-fuselage intersection.

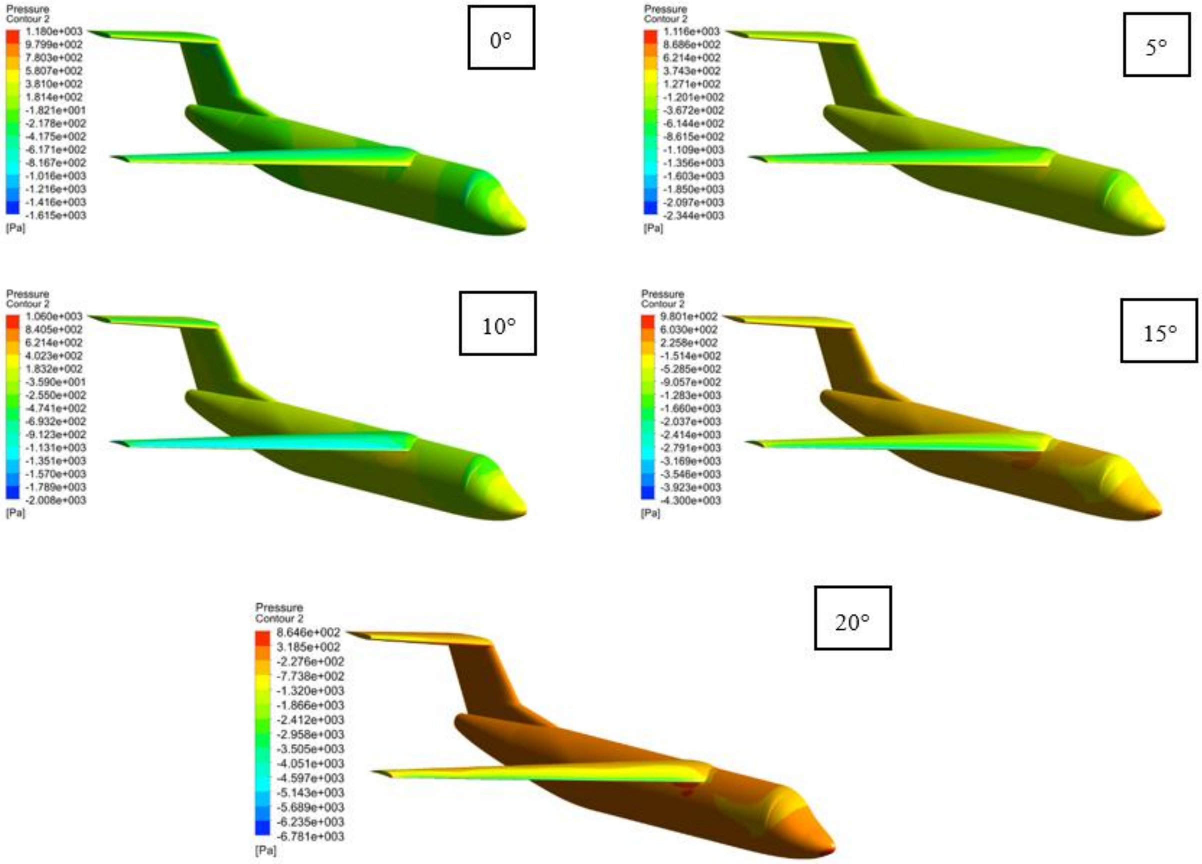

Fig. 12. Pressure contours on the UAV's surface at different AoAs

Velocity contours were obtained at AoA = 0°, 5°, 10°, 15°, and 20° in the midsection of the UAV wing. At AoA = 0°, Figure 13 shows the highest velocity values on the extrados, reaching 40.27 m/s near the mid-chord of the profile. Compared with the other AoA cases, the 0° simulation exhibits the highest overall velocity distribution. This behavior is explained by the fact that increasing AoA leads to a general reduction of velocity magnitude across the wing profile. At AoA = 15°, the highest velocity is concentrated near the wingtip, caused by the limited space available for airflow to reach the trailing edge due to wing inclination. Finally, at AoA = 20°, Figure 13 reveals a marked reduction in velocity along the trailing section of the profile, evidencing airflow disproportion and the generation of vortical trails.

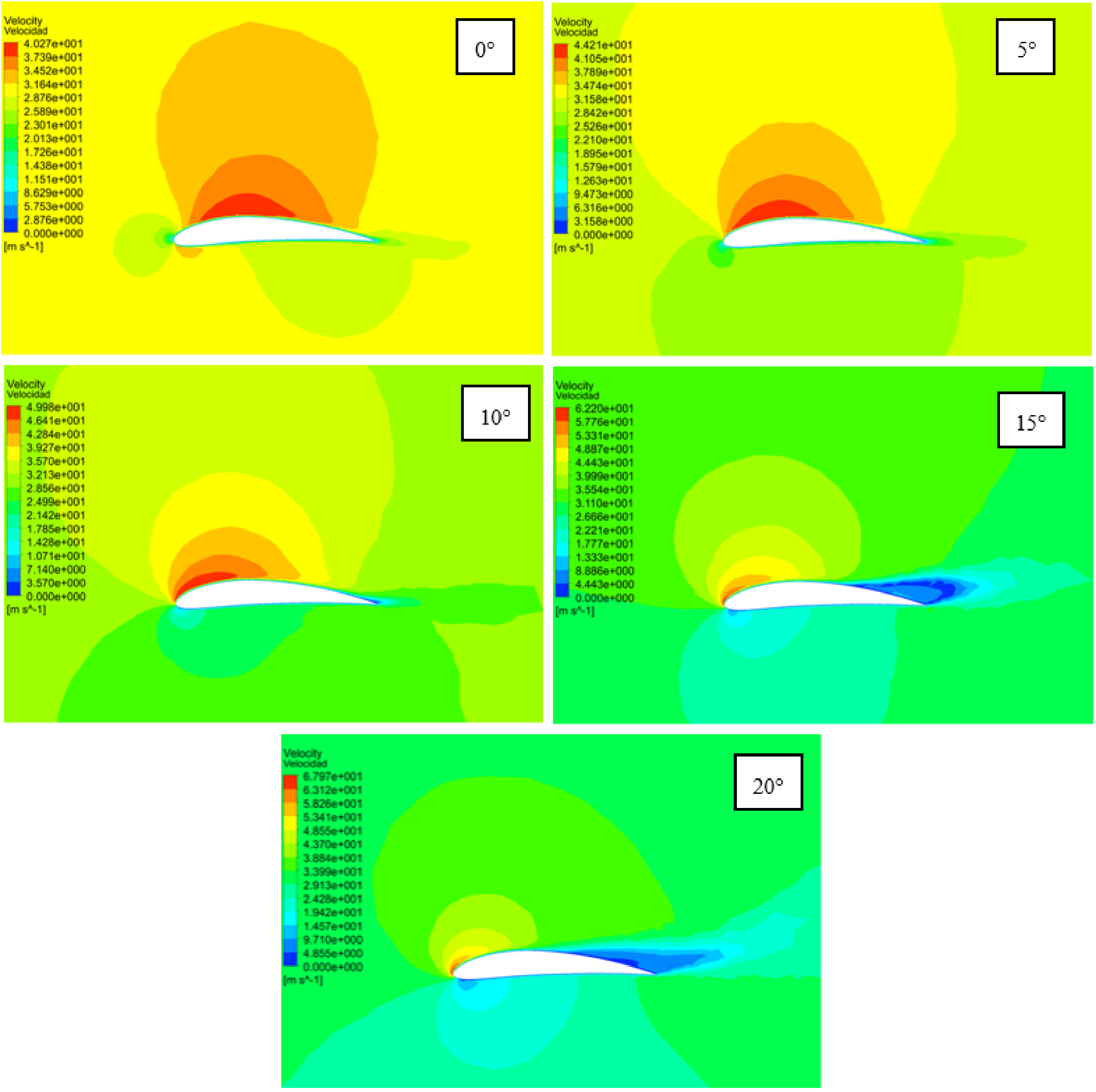

Fig. 13. Velocity contours around the wing's mid-span at different AoAs

4. CONCLUSION

The present work conceptually designs a UAV for firefighting applications equipped with a fire-extinguisher ball release system. The aerodynamic parameters were calculated using the NACA 6412 airfoil, resulting in a UAV with a length of 3.075 m and a wingspan of 3.25 m. A high-wing configuration was selected due to its superior stability compared to mid- and low-wing designs, while a T-tail was chosen to minimize airflow interference. The aerodynamic polar curve was obtained, showing an increase of C_x with C_y.

The fire-extinguisher ball system was designed to allow the UAV to carry 13.5 kg (9 balls of 152 mm), achieving a firefighting effectiveness of 9 m² over a linear range of 90 m. Three case studies were conducted to assess UAV range efficiency: for a range of 3.9 km, the $MTOW$

was calculated as 61.60 kg with an empty UAV weight of 43.87 kg. For a maximum range of 180.01 km with 23.9 L of fuel, the operative $MTOW$ reached 76.51 kg.

CFD simulations at 500 m altitude and 30 m/s airspeed were performed. The simulations provided lift and drag data for AoA values of 0°, 5°, 10°, 15° and 20°. Results indicated that the optimal AoA for operating under the first case $MTOW$ is 5.09°, while the maximum operative $MTOW$ requires an AoA of 7.73°, corresponding to a lift force of 750.27 N. Pressure and velocity contours confirmed that the UAV operates efficiently up to AoA = 10°; however, at AoA = 15°-20°, a significant reduction in lift and an increase in drag occur, indicating stall onset.

Operating in Amazonian environments presents several challenges. High temperatures (>35°C) and humidity levels of 80%-100% may affect UAV electronic components. Future research should therefore focus on selecting more suitable materials, such as carbon-fiber composites. Furthermore, heavy rain could interrupt signal transmission, making it essential to integrate higher-resolution cameras and more robust communication systems.

References

1. Defensoría del Pueblo. 2024. *Informe de supervisión en el marco de los incendios forestales 2024: impacto, responsabilidad y vulneración de derechos fundamentales*. [In Spanish: *Supervisory Report in the Context of the 2024 Forest Fires: Impact, Responsibility, and Violation of Fundamental Rights*]. Lima: Biblioteca Nacional del Perú.
2. Sevzinski D.T., I. Georgiev, H.P. Panayotov, S.I. Penchev. 2019. „Effective use of a helicopter with a Bambi bucket firefighting system in Bulgaria”. In: *IOP Conference Series: Materials Science and Engineering* 664 (1): 012005. IOP Publishing.
3. Sousa V.R., V. Gamboa. 2020. „Aerial Forest fire detection and monitoring using a small UAV”. *KnE Engineering* 5 (6): 242-256. DOI: https://doi.org/10.18502/keg.v5i6.7038.
4. Wu R.Y., X.C. Xie, Y.J. Zheng. 2024. „Firefighting Drone Configuration and Scheduling for Wildfire Based on Loss Estimation and Minimization”. *Drones* 8 (1): 17. DOI: https://doi.org/10.3390/drones8010017.
5. Kau D., M.F. Evliyaoglu, S. Karakus, R. Mörsch, L. Babetto, E. Stumpf. 2022. „DLR design challenge 2022: Next generation firefighting aircraft – FireWASP”. In: *German Aerospace Congress, Dresden, Germany*: 27-29.
6. Sharma L. 2024. „Involvement of drone technology and fire extinguishing balls in firefighting”. *Theory and Practice* 30(5): 2317-2326. DOI: 10.53555/kuey.v30i5.3282.
7. Pawar M.R., B.K. Patle, N. Pagar. 2023. „Design and Development of Fire Fighting Drone”. *International Research Journal of Innovations in Engineering & Technology* 7(12): 249-258.
8. De Moura J.P.A.S. 2021. „Autonomous Targeting System for a Firefighting Drone”. Master’s thesis, Portugal: Universidade de Coimbra.
9. Dieteren S.H.P. 2021. „Application of drone technology for firefighting”. Master’s thesis, Netherlands: University of Twente.
10. Aydin B., E. Selvi, J. Tao, M.J. Starek. 2019. „Use of Fire Extinguishing Balls for a Conceptual System of Drone Assisted Wildfire Fighting”. *Drones* 3 (1): 17. DOI: https://doi.org/10.3390/drones3010017.

11. Artamonova L.G., A.V. Kuznetsov, N.N. Pesotskaya. 2010. *Verification Calculation of Aerodynamic Characteristics of the Aircraft*. Moscow: Moscow Aviation Institute.
12. Aliaga Nestares V., N. Quispe Gutiérrez, I. Ramos Parado, D. Rodríguez Zimmermann. 2018. *Estudio de condiciones atmosféricas favorables a los incendios forestales en el Perú*. [In Spanish: *Study of Atmospheric Conditions Favorable to Forest Fires in Peru*]. Lima: Servicio Nacional de Meteorología e Hidrología del Perú.
13. Raymer D.P. 2012. *Aircraft Design: A Conceptual Approach*. Reston, VA: American Institute of Aeronautics and Astronautics.
14. Kennedy G., J.R. Martins. 2012. „A Comparison of Metallic and Composite Aircraft Wings Using Aerostructural Design Optimization”. In: *12th AIAA Aviation Technology, Integration, and Operations (ATIO) Conference and 14th AIAA/ISSMO Multidisciplinary Analysis and Optimization Conference*: 5475.
15. Jimenez D., E. Valencia, A. Herrera, E. Cando, M. Pozo. 2025. „Evaluation of series and parallel hybrid propulsion systems for UAVs implementing distributed propulsion architectures”. *Drones* 9(2): 63. DOI: https://doi.org/10.3390/aerospace9020063.
16. Diogo C.M.A., E.C. Fernandes. 2024. „A mass, fuel, and energy perspective on fixed-wing unmanned aerial vehicle scaling”. *Drones* 8(8): 396. DOI: https://doi.org/10.3390/drones8080396.
17. Torenbeek E. 1988. *Synthesis of Subsonic Airplane Design*. London: Delft University Press.
18. Chen C., X. Wang, W. Liu, Q. Li. 2023. „Aerodynamic Simulation of a Cargo UAV with Twin-Boom and Rear-Mounted Propeller”. In: *Asia-Pacific International Symposium on Aerospace Technology*: 1490-1503. Springer Nature, Singapore.
19. Valmiki S., M. Chavan, S. Jolada, M. Ladde, M. Mateen. 2024. „Fire Fighting Drone Using Fire Extinguisher Ball”. *Journal of Scientific Research and Technology* 2(7): 27-36. DOI: https://doi.org/10.61808/jsrt117.
20. NASA. „Navier-Stokes Equations”. Available at: https://www.grc.nasa.gov/www/k-12/airplane/nseqs.html.
21. Airforce Technology. „SIRTAP Tactical Unmanned Aerial System (UAS), Spain”. Available at: https://www.airforce-technology.com/projects/sirtap-tactical-unmanned-aerial-system-uas-spain/?cf-view.
22. Aircrafts. „C919”. Available: https://doc8643.com/aircraft/C919.
23. Ramesh P.S., J.M.L. Jeyan. 2022. „Comparative Analysis of Fixed-Wing, Rotary-Wing and Hybrid Mini Unmanned Aircraft Systems (UAS) from the Applications Perspective”. *INCAS Bulletin* 14(1): 137-151.
24. Dhakad A. S., A. Sawarni, G. Sahu, N. Sahu. 2015. „Analysis of NACA 6412 Airfoil (Purpose: Propeller for Flying Bike)”. *IOSR Journal of Mechanical and Civil Engineering (IOSR JMCE)* 12(1): 115-124. DOI: 10.9790/1684-1212115124.
25. Wei Z., J.Li, S. Tang, Z. Yang. 2022. „Investigation and Improvement of T Tail Junction Flow Separation for a Demonstration Aircraft”. *Aerospace* 9(10): 567. DOI: https://doi.org/10.3390/aerospace9100567.
26. Zhao Z., H.Cui. 2022. „Numerical investigation on combustion processes of an aircraft piston engine fueled with aviation kerosene and gasoline”. *Energy* 239: 121848. DOI: https://doi.org/10.1016/j.energy.2021.122264.
27. Wibowo S.B., B. Basuki, S. Sutrisno, T.A. Rohmat, S. Siswantoro, F. Nugroho, P. Ginting, Z. Anwar. 2021. „Vortex Dynamics Study and Flow Visualization on Aircraft Model with Different Canard Configurations”. *Fluids* 6(4): 144. DOI: https://doi.org/10.3390/fluids6040144.

28. Cai M., E. Abbasi, H. Arastoopour. 2013. „Analysis of the performance of a wind turbine airfoil under heavy rain conditions using a multiphase computational fluid dynamics approach”. *Industrial & Engineering Chemistry Research* 52(9): 3266-3275. DOI: https://doi.org/10.1021/ie300877t.
29. ISO 2533:1975. *Standard Atmosphere*. International Organization for Standardization.
30. Anderson J.D. 2021. *Fundamentals of Aerodynamics*. New York: McGraw-Hill.
31. Belligoli Z., S. Guérin, B. Van Oudheusden, R. Dwight. 2019. „Using an anti-fairing to reduce drag at wing/body junctions”. *AIAA Journal* 57(4): 1468-1480. DOI: https://doi.org/10.2514/1.J057481.

Received 06.12.2025; accepted in revised form 24.02.2026